Small Probe Flight Testing of Thermal Protection Systems in Simulated Earth Entries

Adam T. Sidor* , Tyler R. Anderson * and Robert D. Braun †

Georgia Institute of Technology, Atlanta, GA, 30332

Flight testing of thermal protection system materials, once common during the early era of spaceflight, is used infrequently in modern materials development. Testing and qualification of these materials primarily occurs in ground-based facilities which can produce a limited range of discrete test conditions. A small probe platform to test thermal protection system materials in flight can produce environmental conditions that more closely approximate the transient nature of actual entry. A methodology for designing such a test is presented. Test vehicles are designed to be recoverable and are based on the highly stable 45 degree sphere-cone geometry of Mars Microprobe. The current investigation determines the feasibility of simulating low and high energy Earth entries with such a test vehicle launched suborbitally aboard a Black Brant X rocket. Vehicle parameters (mass and maximum diameter) as well as launch and flight trajectories are varied to achieve a range of heat rates and stagnation pressures. An envelope of achievable environmental conditions is generated and compared to those of the reference trajectories. The current design is able to generate peak heat rates on the order of 10^2 W/cm^2 and peak stagnation pressures of 10^1 - 10^2 kPa. Average flow enthalpies of around 4 MJ/kg to 16 MJ/kg can be sustained for anywhere from 10 seconds to 2 minutes.

Nomenclature

C_3	Ratio of ideal to maximum reaction load
C_{D_p}	Parachute drag coefficient
D	Capsule diameter
D_0	Nominal parachute diameter
D_c	Constructed parachute diameter
F	Reaction load
F_{thrust}	Thrust force
h	Altitude
h_0	Specific total enthalpy
h_∞	Specific enthalpy of freestream
I_{sp}	Specific impulse
k	Sutton-Graves constant
M	Mach number
m	Test vehicle mass
m_p	Parachute mass
m_m	Mortar mass
m_{prop}	Propellant mass
m_{struct}	Structural mass
p_0	Stagnation pressure
p_∞	Freestream pressure
$\dot{q}_s$	Stagnation point heat rate
R_n	Nose radius

*Graduate Research Assistant, Guggenheim School of Aerospace Engineering, AIAA Student Member

†David and Andrew Lewis Professor of Space Technology, Guggenheim School of Aerospace Engineering, AIAA Fellow

S/D	Stroke to bore ratio
t_{burn}	Stage burn time
t_{TSI}	Time to third stage ignition
V	Planet-relative velocity magnitude
V_f	Ejection velocity
x_{CG}	Capsule center of gravity in lateral direction
β	Ballistic coefficient
γ	Flight path angle
γ_e	Flight path (elevation) angle at launch
γ_{TSI}	Flight path angle at third stage ignition
γ_{sp}	Ratio of specific heats
λ_0	Latitude at entry interface
ρ	Atmospheric density
ρ_p	Parachute packing density
ψ	Heading angle at entry interface
CG	Center of gravity
IHF	Interaction Heating Facility
IML	Inner mold line
IMU	Inertial measurement unit
ISS	International Space Station
MPCV	Multi-Purpose Crew Vehicle
MSL	Mean sea level
OML	Outer mold line
SRC	Sample Return Capsule
TPS	Thermal protection system
WFF	Wallops Flight Facility

I. Introduction

The advent of thermal protection systems (TPS) for hypersonic entry in the 1950s and 1960s demanded new methods and facilities for testing and qualifying TPS materials in relevant heating conditions. At General Electric, initial tests placed ablative specimens at or near the exhaust plane of a rocket nozzle.[1] A short time later – in the late 1950s – newly adopted electric arc-heated plasma jets expanded testing capability. Complementary to ground-based testing, experimental entry vehicles carried on ballistic missiles (the Mark and RVX series of reentry vehicles) tested new materials in hypersonic flight.[2] On at least one (a General Electric variant of RVX-1 flown in 1959), three different ablative materials were tested simultaneously in a single flight after demonstrating promising results in the laboratory. Two of the RVX vehicles, the General Electric capsule and another flying a TPS designed by Avco Everett Research Laboratory, were recovered for subsequent analysis.[1] Lockheed's X-17, a rocket designed specifically for reentry testing of nosecones, also operated around this time making 26 flights from 1955–1958.[2]

Today, flight testing of TPS as a tool in materials development has largely disappeared due to cost and schedule concerns.[3] Modern TPS flight testing follows extensive ground-based testing and largely occurs on complete or near-complete vehicle designs (e.g., Orion Exploration Flight Test 1). In this current approach, testing and qualification of TPS materials is confined to arc jets, and other ground-based facilities, which attempt to replicate environmental conditions at discrete points within the continuum of entry conditions encountered in flight.

Small entry vehicles have been posited as cost-effective platforms for scientific and engineering testing and exploration.[3,4,5,6,7] One design, Small Probe Reentry Investigation for TPS Engineering (SPRITE), is intended to enable both ground and flight testing of TPS materials.[3,4] Other small entry vehicles are under development with materials testing and validation as an application.[8,9] Suborbital sounding rockets have been proposed, and demonstrated, as launch platforms for hypersonic flight testing in a few recent examples. Sub-Orbital Aerodynamic Reentry EXperiment (SOAREX) has carried a variety of hypersonic experiments over eight flights in the last two decades. One of these experiments, SCRAMP (Slotted Compression Ramp) probe, among other goals, measured temperature, recession and pressure with an instrumented TPS that

remotely transmitted telemetry before splashdown.[10] SHarp Edge Flight EXperiment (SHEFEX) provided model validation for a sharp-edged TPS geometry in hypersonic flight.[11]

Flight testing TPS materials can provide a valuable complement to ground-based testing. Instead of a limited number of discrete environments replicated in the test chamber, materials can be tested in variable conditions that are more representative of hypersonic entry, a "Test Like You Fly" approach. Additionally, repeated flights can establish reliability for new TPS materials speeding infusion into future missions. A small, low cost entry vehicle can facilitate such flight testing. Recovering the capsule, though not required, has the added advantage of post-flight analysis of the ablated TPS. Most of the aforementioned small entry probes are non-recoverable and are not intended to survive. Instead, these designs transmit collected data before ground impact. To the authors' knowledge, a recoverable small probe TPS flight testbed has yet to fly in the current era. This paper seeks to demonstrate the application of such a vehicle to relevant low and high speed entries at Earth.

A. Concept of Operations

The concept of operations for a recoverable, suborbital TPS flight test is shown in Figure 1. The entry vehicle, outfitted with the TPS material(s) under testing, is launched aboard a suborbital rocket. Over its ascent, the rocket is accelerated to a target velocity and altitude. For a high energy entry, the rocket may be pitched down during its trajectory to further increase entry velocity. At the desired separation state, the entry vehicle is deployed from the rocket and exposed to aerodynamic forces and heating. Data collection begins immediately upon separation. A variety of sensors may be used depending on test requirements, e.g., in-depth thermocouples, recession sensors, pressure transducers, and/or an inertial measurement unit (IMU) for post-flight trajectory reconstruction.

The entry vehicle is designed to passively maintain stability throughout the flight, requiring no active guidance or stabilizing devices. Once the vehicle decelerates to subsonic speeds, a parachute is deployed enabling safe landing and recovery. Both the recorded data and TPS material(s) are retrieved for post-flight analysis.

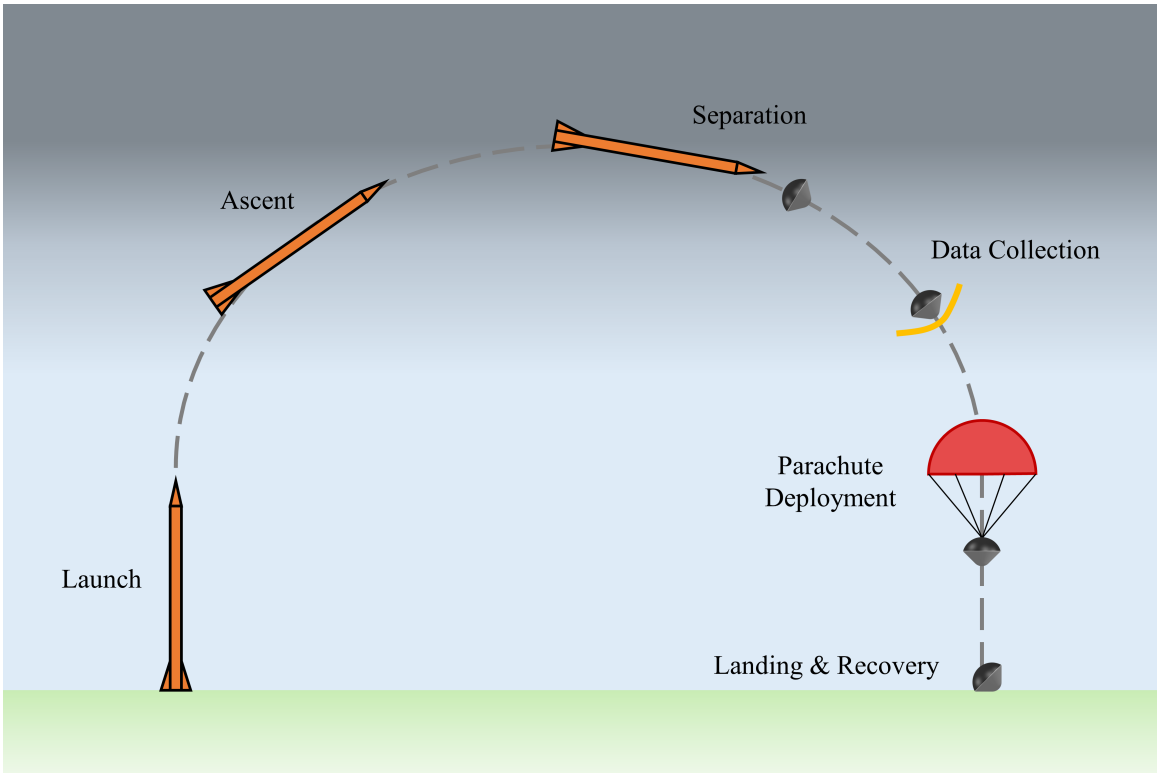

Figure 1. Concept of Operations for Recoverable Small Probe TPS Flight Test Platform

II. Methodology

This research investigates conceptual vehicle and trajectory designs to simulate a portion of two reference entries: (1) a low speed ballistic entry representative of a ballistic return of the Orion Multi-Purpose Crew Vehicle (MPCV) from the International Space Station (ISS) and (2) a high speed ballistic sample return entry based on the Stardust Sample Return Capsule (SRC) entry. A suborbital sounding rocket is used as a launch platform for its low cost and rapid development times.

Designs seek to simulate heating and stagnation pressure over the reference trajectories. Design parameters include test vehicle mass and diameter, launch elevation and the timing and orientation of an exoatmospheric burn – all of which are varied to produce an envelope of relevant test conditions. The capsules are recoverable, though the details of recovery operations are not considered in this study.

A. Test Vehicle

Following past and current small entry vehicle designs, the capsule geometry is a 45 degree sphere-cone based on the Mars Microprobe outer mold line (OML) geometry,[12,13] which exhibits aerodynamic stability throughout all flight regimes given proper center of gravity (CG) placement. The geometry is shown as a function of maximum diameter, D, in Figure 2. Aeroshells are sized to internally accommodate a subsonic parachute, ballast mass and an electronics package for data recording. Note that certain aspects of the capsule design are not varied. For instance, design parameters such as heat shield thicknesses and structural sizing are fixed to plausible values. These aspects of the design are outside the scope of the current study but could be incorporated as additional parameters in future work.

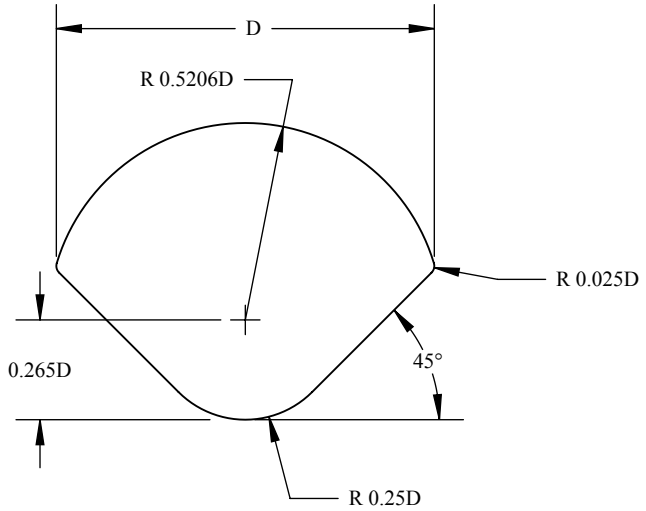

Figure 2. Mars Microprobe 45° sphere-cone outer mold line geometry.

1. *Aeroshell*

An approximate TPS sizing is assumed based on typical flight materials and tailored for the given entry profile. For the relatively benign ISS return, TPS thickness is 1 inch at the nose, 0.5 inch on the flank and 0.25 inch on the aftbody. For the sample return, TPS thickness is 2.0 inch at the nose, 1.0 inch on the flank and 0.5 inch on the aftbody.[a] Flank and aftbody TPS thicknesses reflect reductions in incident heating away from the stagnation point. A 1/16" thick aluminum shell forms the aeroshell sub-structure to which the heat shield is bonded.

[a]The Stardust SRC heat shield was 2.29 inch at the stagnation point.[14] The total heat load of the flight test will necessarily be less than that of the actual SRC due to only a portion of a full trajectory being flown.

2. *Parachute*

A subsonic parachute is deployed to slow the test vehicle to a safe rate of descent. The terminal velocity must be low enough to maintain a largely intact TPS upon landing. Conservatively, we limit terminal velocity to no greater than 6 m/s, a requirement derived from the safe descent rate for U.S. Army paratroopers.[15] A solid conical parachute is the baseline design. The simple construction of conical parachutes consists of triangular gores which are stitched together to form a cone. This type of parachute is inexpensive and offers slightly higher drag performance than flat circular parachutes. Design parameters for a representative vehicle mass are summarized in Table 1.[16]

Table 1. Design parameters for a solid conical parachute assuming 30kg test vehicle.

Parameter	Value	Unit
Test vehicle mass, m	30	kg
Terminal descent rate	6	m/s
Parachute drag coefficient C_{D_p}	0.90	–
Base Angle	25	deg
Parachute constructed diameter, D_c	4.2	m
Parachute nominal diameter, D_0	4.4	m
Parachute mass, m_p	3.6	kg
Mortar mass, m_m	4.2	kg

The parachute mass is estimated using the TWK weight determination method.[17] The canopy is composed of twenty gores. Radial tapes and suspension lines are assumed to be nylon, and each suspension line has a strength of 1000 lbf (4450 N) – sufficient for the vehicle masses in this study. A mortar, which offers reliable and consistent positive inflation, is used for parachute deployment. Mortar mass is difficult to size analytically due to variable configurations of the different components. Instead, its mass is computed as a function of parachute mass, m_p, via an approximate empirical relation:[18]

$$m_m = 2.2\sqrt{m_p} \tag{1}$$

Figure 3(a) shows how recovery system mass scales with the total mass of the test vehicle.

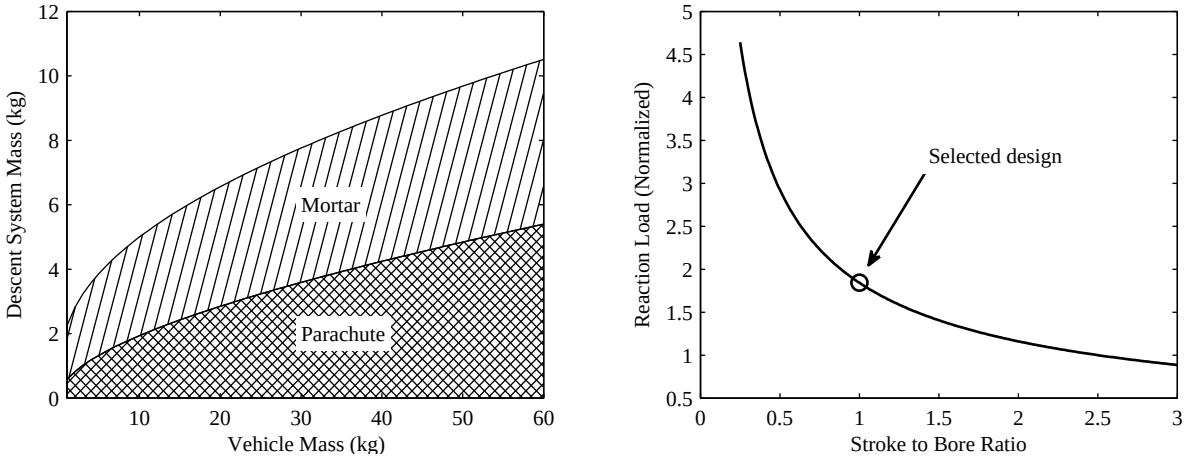

(a) Recovery system mass as a function of total vehicle mass.

(b) Reaction load as a function of stroke to bore ratio.

Figure 3. Recovery system design space.

The parachute can is sized as follows: given a specified test vehicle mass, the parachute and mortar mass is computed as above. Assuming a typical packing density, ρ_p, of 40 kg/m^3, the packed volume of

the parachute is obtained. The entire system is enclosed in an aluminum canister. Specifying a stroke to bore ratio, S/D, that is the ratio of the length of the canister to its diameter, yields the geometry of the recovery system. Previous experience suggests a desired parachute canister stroke to bore ratio, S/D, of 2.5. However, due to the small size of the capsules under consideration, it is desirable to consider smaller ratios of S/D to reduce the overall length of the packed parachute.

To evaluate, reaction load, F, is computed as function of ejection velocity, V_f, the ratio of ideal reaction load to maximum reaction load, C_3 (around 0.7 for real systems due to time-varying acceleration), m_p, ρ_p, and S/D according to an analytical relation found in Ref. 19:

$$F = \frac{V_f^2}{2C_3}\left(\frac{m_p}{S/D}\right)^{2/3}\left(\frac{\pi\rho_p}{4}\right)^{1/3} \tag{2}$$

Reaction load, normalized by the load at $S/D = 2.5$, is plotted against S/D in Figure 3(b). As the canister is flattened, that is S/D is reduced, the reaction load increases. Below $S/D = 1$, that increase becomes significant with reaction load rapidly growing to a few multiples above the nominal value. For this reason, the stroke to bore ratio is selected to be $S/D = 1$, which balances the need for a more compact recovery system without driving the reaction load beyond what could be reasonably accommodated by the structure.

3. Electronics

An electronics package records and stores data during flight. For reference, the Data Acquisition System of SPRITE collects data from a variety of TPS sensors, including thermocouples, ablation sensors and an isotherm detector, mounted in depth at various locations along the heat shield. This package is designed to be contained within the 1U CubeSat form factor (a 10cm x 10cm x 10cm volume). Some miniaturization is considered feasible, thus a 500cm^3 volume for electronics is assumed as the baseline for this study with a uniform density of 500 kg/m^3 (on the order of that of a lithium ion battery) – a 250g package. In practice, electronics components may be rearranged to optimize layout and packaging. To capture this effect, dimensions of the 500 cm^3 volume are allowed to vary – the only constraints being that the total volume requirement must be met and no single dimension can be less than 1cm. The details of wiring sensors to the electronics package are left to future work, but it is reasonable to assume that such additions can be accommodated with little impact on the gross internal layout and total mass.

4. Packaging

The packaging design is implemented as a function of two variables only, maximum vehicle diameter and target mass. The sizing and placement of the subsystems (aeroshell, parachute, and electronics) flows down from this specification in a hierarchical manner with feasibility checks implemented throughout (Figure 5). The OML geometry, following the Mars Microprobe design, is completely defined by the diameter, D, which is subject to a maximum constraint imposed by the payload diameter of the launch vehicle. Likewise, the TPS thicknesses given above are fixed offsets from the OML, thus defining the inner mold line (IML), and the structural shell is a fixed offset from the IML.

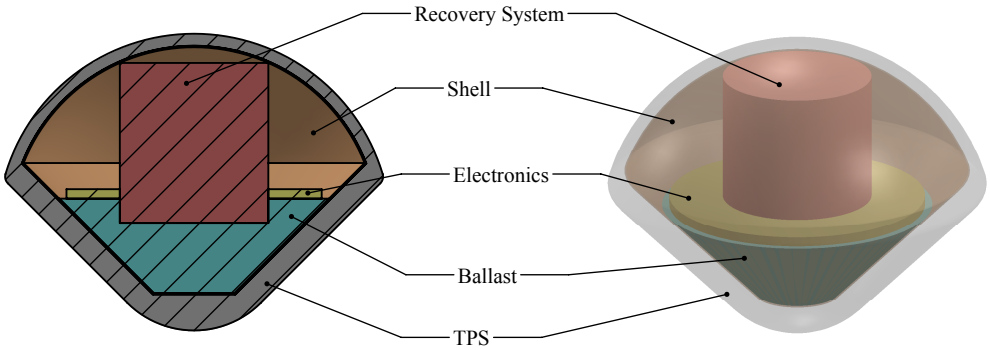

Figure 4. Representative capsule design with typical subsystem layout.

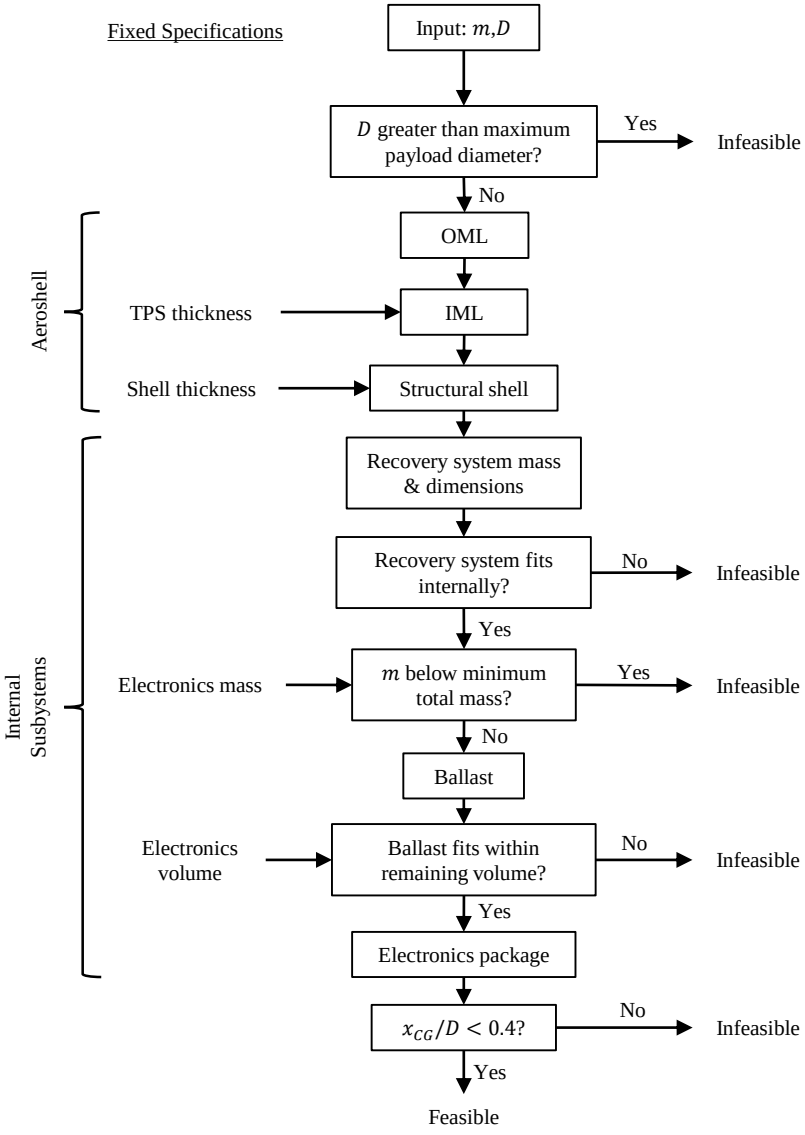

Figure 5. Flow chart of packaging design.

Layout of the internal subsystems follows from the aeroshell geometry. Recovery system size and mass is computed from the total vehicle mass and is positioned as far aft as possible, coincident with the backshell (the design is infeasible if the parachute canister cannot fit within the aeroshell). The combined mass of the aeroshell, recovery system and electronics represent a minimum feasible vehicle mass. If the specified target mass is less than the minimum mass, then the design is infeasible. If the target mass is greater than or equal to the minimum mass, the design may proceed. A tungsten ballast is used to raise the base mass to the desired target. Assuming the ballast does not exceed the remaining available volume, the electronics are the last subsystem added, directly above the ballast. The volume for the electronics package is allocated symmetrically about the centerline with a height of 1cm. Lastly, the lateral CG location, x_{CG}, is checked against that required for static stability – we require $x_{CG}/D < 0.4$ based on the REBR design.[7]

B. Launch Platform

The launch platform is the Black Brant X, a suborbital rocket operated through the NASA Sounding Rockets Program Office (SRPO). Its third, and final, stage operates exoatmospherically and can be oriented before the burn to control the flight trajectory, a capability demonstrated in a at least one recent flight experiment.[20] A overview of this and other sounding rockets is available in the NASA Sounding Rocket Program Handbook.[21] Average stage performance metrics and mass properties of the Black Brant X are outlined in Table 2[b]. The entire 3-stage assembly has a mass of 2570.5 kg (5667 lb) and a 17.26 inch nominal payload diameter.

Table 2. Black Brant X average stage performance and mass properties.

Stage	Type	I_{sp} (sec)	t_{burn} (sec)	F_{thrust} (kN)	m_{prop} (kg)	m_{struct} (kg)
1	Terrier MK12 Mod 1	200	4.4	257.5	578	322
2	26KS 20,000 Black Brant V	208	26.9	75.7	997	268
3	Nihka	256	16.125	53.4	342.9	62.6

1. *Launch site and launch parameters*

Test flights are launched from sea level from the Wallops Flight Facility (WFF) located at 37.9402°N, 75.4664°W. Any of the 20,000 lb rated launchers available at WFF would support the mass requirement for this mission. The 20 K Launcher with 37 foot boom length is the baseline for this work.[21] The initial launch vector is oriented due east in azimuth. Launch elevation angle is allowed to vary, though in practice a launch elevation that is too shallow will result in an infeasible design – the rocket must leave the atmosphere in order for the third stage to be oriented and fired.

C. Atmosphere

The 1976 U.S. Standard Atmosphere is used to generate atmospheric properties between sea level and 86km. Above 86km, an exponential atmosphere model is used. The atmospheric model is depicted in Figure 6 with freestream density and pressure plotted across altitude above mean sea level (MSL).

D. Simulation

Three-degree-of-freedom, ballistic (non-lifting) trajectories are simulated via equations of motion adapted from Ref. 22, formulated in a planet-centric, planet-fixed frame. A uniform, spherical, rotating planet with atmosphere at rest relative to the planet is assumed. Stagnation point convective heating is approximated from the Sutton-Graves relation reproduced in Eq. (3) where ρ is the local atmospheric density and R_n is the capsule nose radius.[23] The constant k is atmosphere-dependent (at Earth, $k = 1.7415 \times 10^{-4}$ kg$^{1/2}$m^{-1}).

$$\dot{q}_s = k \left(\frac{\rho}{R_n} \right)^{1/2} V^3 \tag{3}$$

[b]Supplemental data was obtained from the Encyclopedia Astronautica, URL: www.astronautix.com.

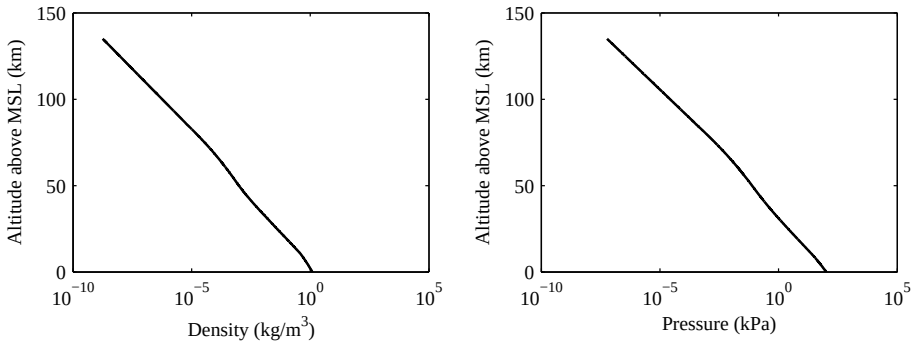

Figure 6. Models of freestream atmospheric density and pressure.

Radiative heating is assumed to be negligible for the low energy, suborbital entries of this study. However, for the sample return reference trajectory where radiative heating is non-negligible, data are supplemented with high fidelity results from the literature.

The ratio of stagnation pressure to freestream pressure, p_0/p_∞, is approximated via the normal shock relations for a calorically perfect gas, Eq. (4), available from several sources (e.g., Ref. 24). This approximation underestimates the true stagnation pressure by a few percent in the hypersonic regime but allows the use of the computationally efficient closed form equation which is a function of Mach number, M, and the ratio of specific heats, γ_{sp}, where $\gamma_{\text{sp}} = 1.4$ for air.

$$\frac{p_0}{p_\infty} = \left[\frac{(\gamma_{\text{sp}}+1)M^2}{(\gamma_{\text{sp}}-1)M^2+2}\right]^{\gamma_{\text{sp}}/(\gamma_{\text{sp}}-1)} \left[\frac{\gamma_{\text{sp}}+1}{2\gamma_{\text{sp}}M^2-(\gamma_{\text{sp}}-1)}\right]^{1/(\gamma_{\text{sp}}-1)} \left[1+\frac{\gamma_{\text{sp}}-1}{2}M^2\right]^{\gamma_{\text{sp}}/(\gamma_{\text{sp}}-1)} \tag{4}$$

Finally, total flow enthalpy, h_0, is computed for comparison to ground-based facilities – that is, NASA Ames Research Center Interaction Heating Facility (IHF). Total enthalpy is a function of freestream enthalpy, h_∞, and the velocity of the incoming flow, which is equal to the planet-relative velocity, V:

$$h_0 = h_\infty + \frac{V^2}{2} \tag{5}$$

E. Reference Trajectories

The two reference trajectories considered in this study are outlined in Table 3. Consistent with a uniform, spherical planet, trajectories are longitude-independent, so this parameter is ignored. The sample return trajectory is based on the Stardust SRC entry. The design trajectory for the Stardust SRC heat shield used a 12.6 km/s entry velocity, 8° entry flight path angle and a ballistic coefficient, β – the ratio of mass to drag area – of 70 kg/m^2 producing a peak stagnation point heat rate of 1200 W/cm^2 about one minute into entry. During mission design, aerothermodynamics were computed with a high fidelity, coupled radiation and ablation code, the results of which were used to set arcjet test conditions for TPS qualification.[25] Radiative heating is non-negligible up through 76s after entry interface, contributing about 10% of the total heat rate near the stagnation point at peak heating. Later work leveraged advances in radiation modeling to refine aeroheating estimates.[26] Radiation from the flow contributes to overall heating both by its incidence on the capsule and through absorption by the flow itself, which augments convective heating. The current work does not seek to replicate these results. Instead, a least squares regression of the literature results is used for the initial portion of the trajectory (up to $t = 76$ sec) where radiative heating is significant, and the CFD results are available. The regression model has the functional form,

$$\dot{q}_s = C R_n^{-\frac{1}{2}} \rho_\infty^m V^n \tag{6}$$

Table 3. Initial state at atmospheric interface, vehicle parameters, and peak conditions for reference trajectories.

Parameter	Unit	ISS return	Sample return
State at atmos. interface			
h	km	125	135
λ	deg	0	42
V	km/s	7.6	12.6
γ	deg	-1.4	-8
ψ	deg	51.6	-7
Vehicle			
β	kg/m^2	407	70
R_n	m	6.0	0.2286
Peak conditions			
$\dot{q}_s$	W/cm^2	46.2	1090
p_0	kPa	70.0	36.3

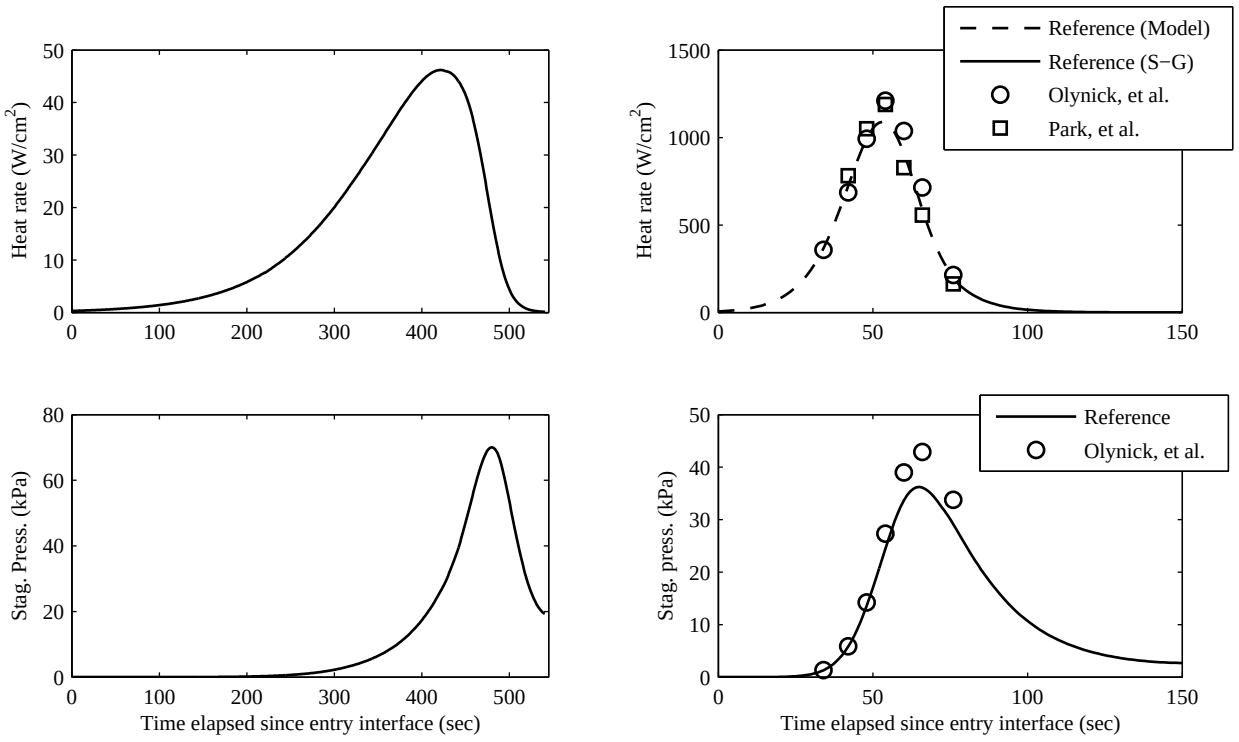

(a) ISS return

(b) Sample return

Figure 7. Stagnation point heat rate and stagnation pressure for reference trajectories.

where C, m, and n are the independent variables. Stagnation point heating for the sample return reference trajectory is shown in Figure 7(b). The region where the regression model is applied is indicated. Results from the literature are shown for comparison.

The ISS return reference trajectory is based on a ballistic return of the Orion MPCV from the ISS. The MPCV is a truncated spherical segment of 6-meter radius with a landing mass of 20,500 lbs (9299 kg).[27] Ballistic coefficient is 407 kg/m^2. Heat rate and stagnation pressure profiles for the ISS return trajectory are shown in Figure 7(a). The maximum heat rate is significantly lower than that of the sample return mission largely due to substantially larger nose radius and lower entry velocity.

F. Flight Test Design

Independent variables controlled by the simulation include vehicle parameters (vehicle mass, m, and maximum diameter, D), launcher orientation (elevation angle, γ_e) and the 3rd stage burn (time of ignition, t_{TSI}, and flight path angle at ignition, γ_{TSI}). Recall that the 3rd stage operates exoatmospherically, therefore the rocket must coast for a period of time, t_{TSI}, after 2nd stage burnout before igniting the 3rd stage. However, if t_{TSI} is too long, the rocket will reenter before the 3rd stage can fire.

Table 4. Flight test constraints by category.

Category	Parameter	Unit	Lower bound	Upper bound
Test vehicle	m	kg	N/A	N/A
	D	m	N/A	0.425
Launcher	γ_e	deg	63	89
3rd Stage	γ_{TSI}	deg	-180	180
	t_{TSI}	sec	56	370
	h	km	125	unbounded

Constraints on the independent variables are summarized in Table 4. As discussed earlier, the test vehicle design is constrained by packaging and mass considerations. Note that all but one of the constraints on the vehicle design cannot be reduced to a lower and upper bound. The payload diameter of the sounding rocket imposes a maximum on the test vehicle diameter. Other constraints on m and D are discussed further below. For practical reasons, side constraints are imposed on the remaining independent variables to further bound the design space and reduce computation time. These bounds are derived from the requirement that the 3rd stage be operated exoatmospherically, and are defined such that no feasible designs are inadvertently eliminated. Exoatmospheric interface is assumed at 125km, thus altitude must remain above that during the third stage burn.

III. Results

A. Vehicle Design

The packaging approach outlined in Figure 5 produces a set of feasible vehicle designs in the mass-diameter space (Figure 8). Feasible test vehicles range from approximately 0.3 m to 0.425 m in diameter and 7 kg to 64 kg in mass for the ISS return, and from 0.34 m to 0.425 m and 10 kg to 38 kg for the sample return. These vehicles range in ballistic coefficient from 73.5 kg/m^2 to 355.3 kg/m^2 and from 81.4 kg/m^2 to 251.6 kg/m^2 for the ISS return and the sample return, respectively. The upper boundary of the feasible region is exclusively dominated by recovery system size – that is, where the parachute canister is too large for the capsule. At the lower boundary of the feasible region, a band of statically unstable designs exists. Immediately below those designs are those vehicles that violate the minimum mass requirement. Lastly, maximum payload diameter constrains the right boundary of the feasible space.

The range of feasible vehicle designs is more limited in the sample return case due to the a priori assumption of larger TPS sizing. The TPS consumes a larger portion of the total capsule volume leaving less space for the internal components. The recovery system, which is large and relatively inflexible in terms of its geometry, thus imposes a more substantial constraint on the feasible region, a result which is evident from the comparison in Figure 8. The upper constraint boundary is shifted down and to the right for the

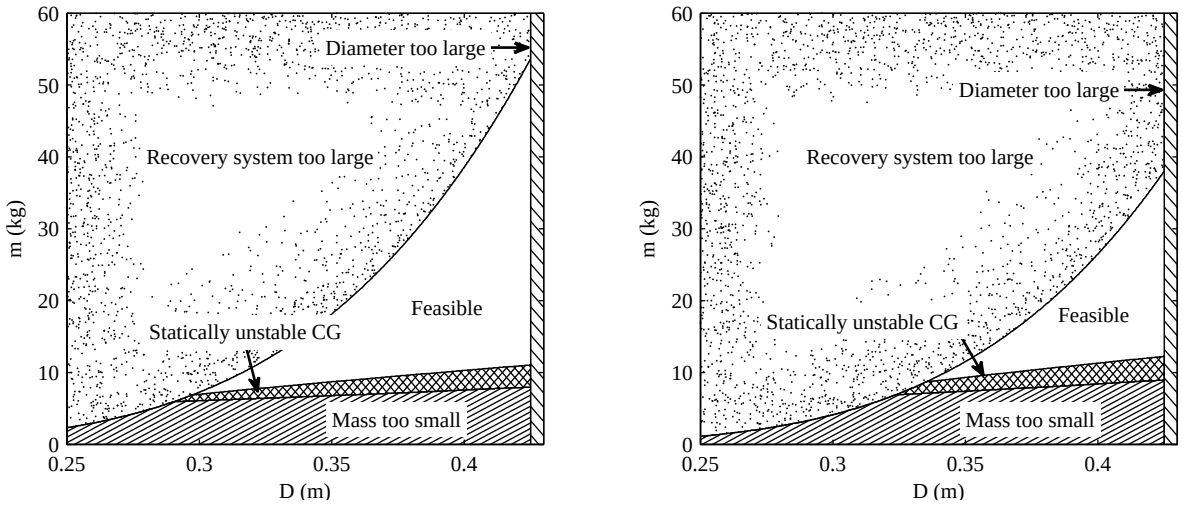

(a) ISS return

(b) Sample return

Figure 8. Feasible and infeasible test vehicle designs in mass-diameter space for both reference trajectories.

sample return flight. This shift represents nearly all of the reduction in the feasible region.

For the chosen OML, nose radius is a fraction of the total diameter and heat rate is inversely proportional to nose radius. Therefore, the sample return test vehicle is more limited in its ability to produce high heat rates due to a larger minimum diameter. This exposes a shortcoming of the current methodology – a thicker TPS was chosen with the assumption that higher heat rates (and heat loads) would require it, but increasing TPS size actually decreases the capability to achieve the desired heating. This shortcoming could be addressed by considering modifications to the OML and/or allowing for more flexibility in the packaging of the recovery system. Allowing nose radius to be reduced from the initial specification ($0.25D$) would augment heating; however, further aerodynamic analysis would be required to assess vehicle stability. Different OML geometries entirely could also be considered – e.g. a sphere-cone design with a narrower cone angle. These investigations are left to future work.

B. Flight Test Environments

Flight tests were generated by a uniform random sampling of the feasible space in order to approximate the envelope of achievable environmental conditions. In total, 1000 flight tests were randomly generated. For clarity, a subset of 100 flight tests is compared to the reference trajectories in Figure 9. Results from all simulations are included in Figures 10 and 11.

1. Heat rate and stagnation pressure

Figure 9 shows stagnation pressure as a function of stagnation point heat rate for the supersonic portion of the trajectory. Trajectories move in a counterclockwise direction from their starting point near the origin. Thus, peak heat rate occurs first, then peak stagnation pressure. Then, as the vehicle decelerates further, both heat rate and stagnation pressure decline rapidly toward the origin again (though stagnation pressure does not go to zero). For clarity and discussion, a single flight test is highlighted in red.

It is clear that the envelope of environmental conditions produced by the flight tests cannot fully capture either reference trajectory. While the range of stagnation pressures is easily spanned by the flight tests, the heat rates cannot be accurately matched. This difficulty was somewhat anticipated due to selection of two extremes of reference trajectory: a low heat rate and high heat rate entry.

The ISS return trajectory is better matched than the sample return trajectory – all but a small gap near peak heating can be reproduced by flight tests (Figure 9(a)). The gap is a consequence of the different OML geometries of the MPCV and the flight test vehicle. That is, while feasible test vehicles have ballistic

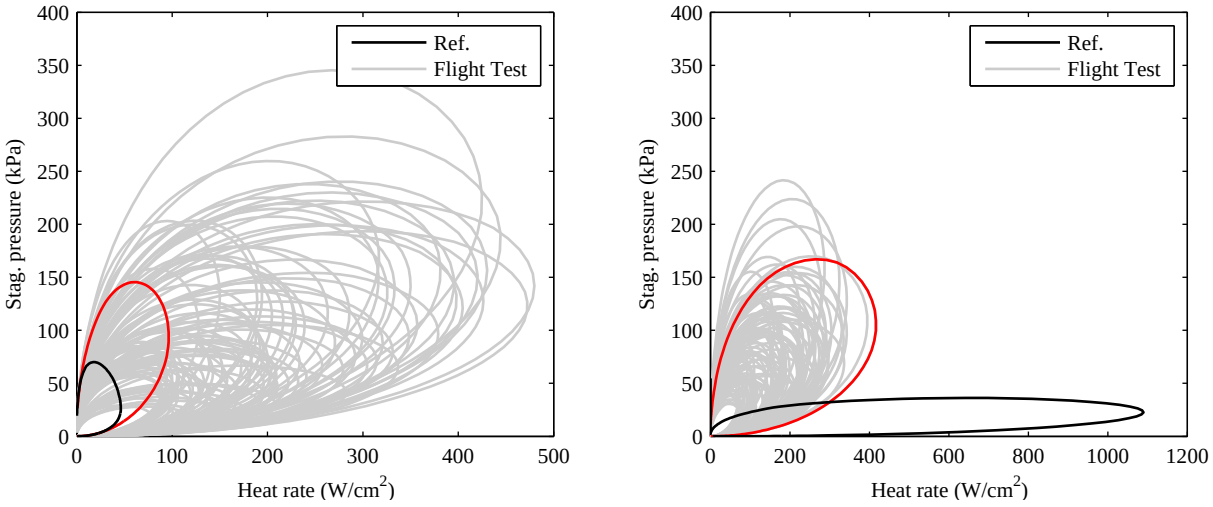

(a) ISS return (b) Sample return

Figure 9. Stagnation point heat rate and stagnation pressure for flight tests and reference trajectories with representative test highlighted (red).

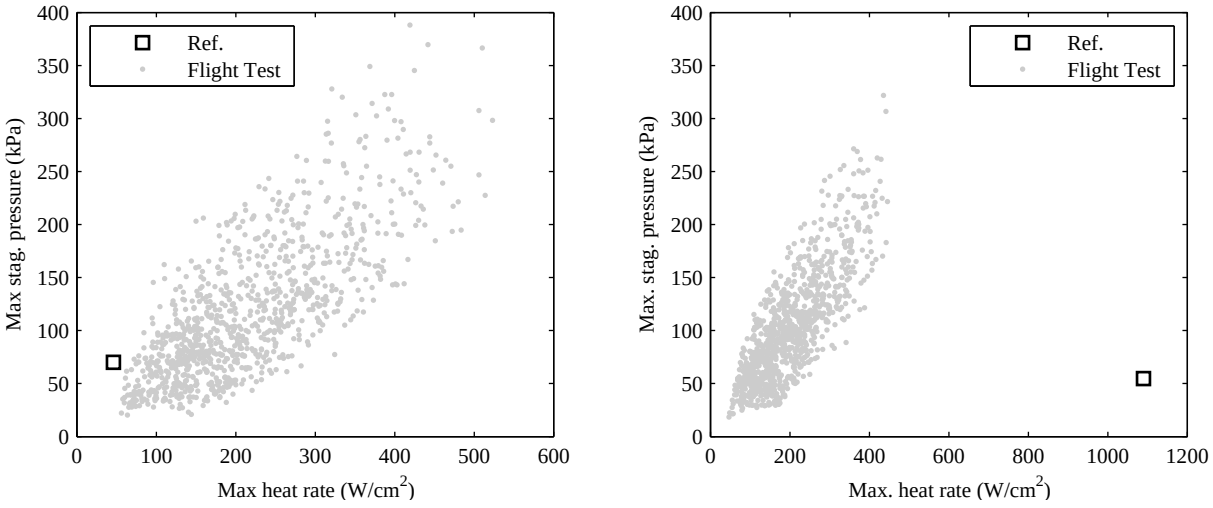

(a) ISS return (b) Sample return

Figure 10. Maximum stagnation point heat rate and maximum stagnation pressure for flight tests and reference trajectories.

coefficients comparable to that of the MPCV, the MPCV has a much larger nose radius which substantially reduces heating. Still, much of the reference trajectory can be reproduced, albeit at discrete points and with multiple flights. A single flight would be better suited to the goal of testing TPS materials in a representative continuous trajectory rather than simply matching conditions at discrete trajectory points. In this case, the highlighted flight (red) in Figure 9(a) closely matches both the initial and final portions of the reference trajectory. The middle portion of the flight test exceeds the reference conditions; however, such a flight would be conservative for the given mission, perhaps desirable for demonstrating margin in the design. Parameters for the selected flight test are outlined in Table 5. The test vehicle is at the upper end of mass and diameter. The rocket launch is near vertical with a relatively early third stage burn oriented toward the Earth at a -48.7° angle relative to the local horizontal.

Table 5. Parameters for selected ISS return flight test.

Category	Parameter	Value
Test vehicle	m	48.3 kg
	D	0.417 m
Launcher	γ_e	88.6°
3rd Stage	γ_{TSI}	-48.7°
	t_{TSI}	101.2 sec

For the sample return trajectory, no flight test can exceed, or even meet, the peak heat rate of the reference mission (Figure 9(b)). A significant energy gap exists between a suborbital entry and an entry from interplanetary flight, which poses a challenge for generating comparable heat rates. As a result, a significant portion of the trajectory is missed. For example, the highlighted trajectory follows the reference for a brief initial period, but then substantially deviates from it for the remainder of the flight. A suborbital flight test as designed, then, is not appropriate for testing TPS materials in this scenario. As discussed previously, relaxing the design constraints by considering alternative packaging arrangements and/or modifications to the OML may improve the ability to test high heat rates.

Ranges of peak environmental conditions are illustrated in Figure 10. In the ISS return scenario, flight tests can generate peak heat rates around 50 W/cm^2 to 500 W/cm^2 and peak stagnation pressures around 20 kPa to 350 kPa (Figure 10(a)). The range of achievable peak conditions is diminished somewhat by the reduction in the feasible vehicle design space for the sample return. Flight tests can generate peak heat rates around 50 W/cm^2 to 420 W/cm^2 and peak stagnation pressures around 20 kPa to 250 kPa in this case (Figure 10(b)). The relationship exhibits a roughly linear trend with peak stagnation pressure increasing with peak heat rate. Again, the peak stagnation pressure of both reference trajectories falls within the capability of the flight tests but the peak heat rate does not. Thus, the flight test, as designed, is best suited to simulating entries with midrange heating conditions, i.e. entries from LEO and with a nose radius comparable to that of the test vehicle ($R_n \approx 7$ cm – 10 cm).

2. *Enthalpy*

Total flow enthalpy is large and relatively constant during the first few seconds to minutes of entry while the vehicle is traveling hypersonically and significant deceleration has yet to occur. During this "high enthalpy" period, flow velocity is the dominant contribution to total enthalpy. Here, this interval is defined as the portion of the trajectory where enthalpy is at least 95% of its peak value. Average enthalpy over the interval is plotted against its duration in Figure 11. Enthalpies generated by the flight tests range from approximately 4 MJ/kg to 16 MJ/kg – somewhat more limited than that of modern ground-based facilities. For example, the IHF arc jet operates at flow enthalpies of 7 to 47 MJ/kg [c]. High enthalpy levels are typically sustained for anywhere from 10 seconds to 1 minute, though in some cases longer durations of up to about 100 seconds are possible.

It is obvious that the energy of a suborbital flight test falls well short of that of the orbital entries. Thus, the peak enthalpies generated in both the ISS return and sample return trajectories are beyond the capability of the current flight tests. However, the suborbital flight test could perhaps provide a useful simulation of enthalpy for the lower energy portions of an orbital entry.

[c]Interaction Heating Facility (IHF) capabilities obtained from http://www.nasa.gov/content/interaction-heating-facility/.

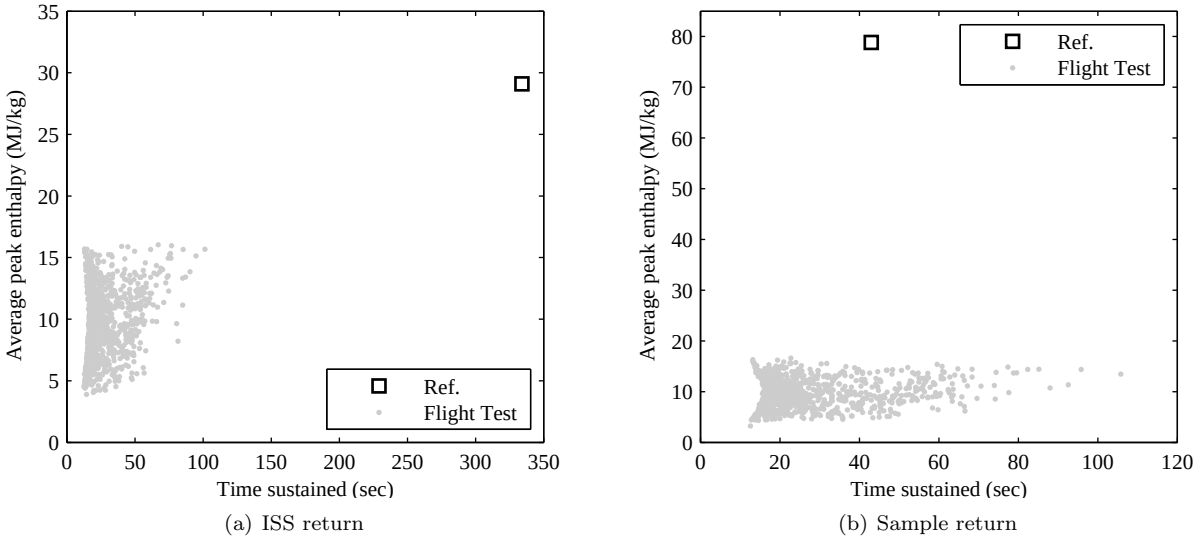

(a) ISS return (b) Sample return

Figure 11. Average of peak enthalpy and duration.

IV. Conclusion

Historically, flight testing of TPS materials provided insight into the performance of materials in representative flight environments – transient conditions beyond the capabilities of ground-based facilities. Such testing is now rare due largely to cost and schedule issues. This work outlines a methodology for designing recoverable, suborbital flights to simulate the conditions of relevant low energy and high energy Earth entries in hypersonic flight. Using a 45° sphere-cone capsule design based on the Mars Microprobe, a process was developed to size and package a recovery system, ballast and electronics within size and CG constraints. Suborbital flight tests, aboard the Black Brant X rocket, were then simulated to generate heat rate, stagnation pressure, and enthalpy profiles.

While exactly matching the reference trajectories proved challenging given the energy difference between a suborbital and an orbital flight, the current design is most suited to the ISS return entry where a flight test can be designed to expose the TPS to peak conditions slightly beyond that of the actual entry – allowing flight qualification with some margin. The high energy, high heat rate of the sample return entry is impossible to achieve within the limits of the current design. Therefore, these flight tests are most appropriate for midrange entries between the extremes of the reference trajectories – peak heat rates on the order of 10^2 W/cm^2 and peak stagnation pressures of 10^1 - 10^2 kPa are achievable. In addition, flow enthalpies of between 4 MJ/kg to 16 MJ/kg are possible – on the lower end of that of a ground-based arc jet facility.

Future work can further establish the capability of recoverable flight testing in simulating Earth entries. Extensions to the current approach could increase flexibility (e.g., by incorporating variable TPS and structural sizings and by allowing a range of S/D ratios for the recovery system) or improve fidelity (e.g., replacing the relatively low fidelity models utilized here with higher fidelity ones). In addition, other capsule geometries, perhaps with sharper nose radii, could be utilized to expand the range of achievable test conditions. Alternative launch vehicles, such as air-launched systems, may provide additional capability. Ultimately, optimization can be employed to design a test flight to best match the environmental conditions of an arbitrary reference entry. Finally, further effort is required to develop a plan for recovery operations including an evaluation of landed footprint dispersion. Air retrieval could be considered to minimize damage to the TPS from impact.

Acknowledgments

This work was supported under NASA grant NNX14AL53H.

References

[1]Sutton, G. W., "The Initial Development of Ablation Heat Protection, An Historical Perspective," *Journal of Spacecraft and Rockets*, Vol. 19, No. 1, 1982, pp. 3–11.

[2]Conley, J. L. and Peterson, K., "What are the Origins of Thermal Protection Systems?" Lecture at Georgia Institute of Technology, April 2011, URL: http://hdl.handle.net/2060/20110023700.

[3]Howard, A. R., Cassell, A. M., and Venkatapathy, E., "Small Probes As Flight Test Beds for Thermal Protection Materials," *7th International Planetary Probe Workshop*, Barcelona, Spain, 2010.

[4]Empey, D., Gorbunov, S., Skokova, K. A., Agrawal, P., Swanson, G., Prabhu, D., Mangini, N., Peterson, K., Winter, M., and Venkatapathy, E., "Small Probe Reentry Investigation for TPS Engineering (SPRITE)," *50th AIAA Aerospace Sciences Meeting*, Nashville, TN, 2012.

[5]Ailor, W. H., Carroll, J. A., Rasky, D. J., and Ridenoure, R., "Pico Reentry Probes: Partnership Pushes Evolution," *AIAA Space Conference & Exposition*, San Jose, CA, 2006.

[6]Ailor, W. H., Dupzyk, I., Shepard, J., and Newfield, M., "REBR: An Innovative, Cost-Effective System for Return of Reentry Data," *AIAA Space Conference & Exposition*, Long Beach, CA, 2007.

[7]Weaver, M. A. and Ailor, W. H., "Reentry Breakup Recorder: Concept, Testing, Moving Forward," *AIAA Space Conference & Exposition*, Pasadena, CA, 2012.

[8]Sidor, A. T., Braun, R. D., and DePasquale, D., "RED-Data2 Commercial Reentry Recorder: Size Reduction and Improved Electronics Design," *AIAA Atmospheric Flight Mechanics Conference*, National Harbor, MD, 2014.

[9]Sakraker, I., Umit, E., Scholz, T., Testani, P., Baillet, G., and Van der Haegen, V., "QARMAN: An atmospheric entry experiment on cubesat platform," *32nd AIAA Applied Aerodynamics Conference*, Atlanta, GA, 2014.

[10]White, B., Morgan, H., and Murbach, M., "SOAREX-VI Re-entry Flight Test Experiment - Electronic Systems of the Slotted Compression RAMP (SCRAMP) Probe," *5th International Planetary Probe Workshop*, Bordeaux, France, 2007.

[11]Eggers, T., Longo, J. M. a., and Turner, J., "The SHEFEX Flight Experiment - Pathfinder Experiment for a Sky Based Test Facility," *14th AIAA/AHI Space Planes and Hypersonic Systems and Technologies Conference*, Canberra, Australia, 2006.

[12]Mitcheltree, R. A., Moss, J. N., Cheatwood, F. M., Greene, F. A., and Braun, R. D., "Aerodynamics of the Mars Microprobe Entry Vehicles," *Journal of Spacecraft and Rockets*, Vol. 36, No. 3, 1999, pp. 392–398.

[13]Braun, R. D., Mitcheltree, R. A., and Cheatwood, F. M., "Mars microprobe entry-to-impact analysis," *Journal of Spacecraft and Rockets*, Vol. 36, No. 3, 1999, pp. 412–420.

[14]Covington, M. A., Heinemann, J. M., Goldstein, H. E., Chen, Y. K., Terrazas-Salinas, I., Balboni, J. A., Olejniczak, J., and Martinez, E. R., "Performance of a Low Density Ablative Heat Shield Material," *Journal of Spacecraft and Rockets*, Vol. 45, No. 2, 2008, pp. 237–247.

[15]"Non-Steerable Troop Parachute System," Airborne Systems, URL: http://www.airborne-sys.com/files/pdf/t-11$_s pec_s heet.pdf$.

[16]Ewing, E. G., Bixby, H. W., and Knake, T. W., "Recovery Systems Design Guide," Tech. Rep. AFFDL-TR-78-151, 1978.

[17]Knacke, T. W., *Parachute Recovery Systems Design Manual*, Para Publishing, Santa Barbara, CA, 1991.

[18]Christian, J. A., Wells, G., Lafleur, J., Manyapu, K., Verges, A., Lewis, C., and Braun, R. D., "Sizing of an Entry, Descent, and Landing System for Human Mars Exploration," *AIAA Space Conference & Exposition*, San Jose, CA, 2006.

[19]Pleasants, J. E., "Parachute Mortar Design," *Journal of Spacecraft and Rockets*, Vol. 11, No. 4, 1973, pp. 246–251.

[20]Wescott, E. M., Stenbaek-Nielsen, H., Conde, M., Larsen, M., and Lummerzheim, D., "The HEX experiment: Determination of the neutral wind field from 120 to 185 km altitude near a stable premidnight auroral arc by triangulating the drift of rocket-deployed chemical trails," *Journal of Geophysical Research: Space Physics*, Vol. 111, No. 9, 2006, pp. 1–11.

[21]"NASA Sounding Rocket Program Handbook," National Aeronautics and Space Administration, 2005, Doc. No. 810-HB-SRP.

[22]Vinh, N. X., Busemann, A., and Culp, R. D., *Hypersonic and Planetary Entry Flight Mechanics*, The University of Michigan Press, 1980.

[23]Sutton, K. and Graves, R. a., "A general stagnation-point convective heating equation for arbitrary gas mixtures," Tech. Rep. NASA TR R-376, 1971.

[24]Anderson, J. D., *Modern compressible flow with historical perspective*, McGraw Hill, 3rd ed., 2003.

[25]Olynick, D., Chen, Y.-K., and Tauber, M. E., "Aerothermodynamics of the Stardust Sample Return Capsule," *Journal of Spacecraft and Rockets*, Vol. 36, No. 3, 1999, pp. 442–462.

[26]Park, C., "Calculation of Stagnation-Point Heating Rates Associated with Stardust Vehicle," *Journal of Spacecraft and Rockets*, Vol. 44, No. 1, 2007, pp. 24–32.

[27]"Orion Quick Facts," National Aeronautics and Space Administration, URL: http://www.nasa.gov/sites/default/files/atoms/files/fs-2014-08-004-jsc-orion_quickfacts-web.pdf.